Results in Surfaces and Interfaces 11 (2023) 100123

Contents lists available at ScienceDirect

Results in Surfaces and Interfaces

journal homepage: www.elsevier.com/locate/rsurfi

Enhanced optoelectronic and supercapacitive performance of electrodeposited Mn_3O_4 thin film prepared from two-electrode: An effect of Zn-ion incorporation

L.O. Animasahun [a], V.A. Owoeye [b], K.O. Olumurewa [c], W. Buremoh [d], H.K. Busari [e], Y.A. Ajayeoba [f], M.M. Popoola [f], J.T. Adeleke [f], S.A. Adewinbi [f,*]

[a] Department of Physics, Electronics and Earth Sciences, Fountain University, Osogbo, Nigeria
[b] Department of Physical and Chemical Sciences, Elizade University, Ilara-Mokin, Nigeria
[c] Department of Physical and Computer Science, McPherson University, Ogun State, Nigeria
[d] Department of Physics and Engineering Physics, Obafemi Awolowo University, Ile-Ife, Nigeria
[e] Department of Pure and Applied Chemistry, Osun State University, Osogbo, Osun State 210001, Nigeria
[f] Department of Physics, Osun State University, Osogbo 210001, Nigeria

ARTICLE INFO

Keywords:
Zn-doped Mn_3O_4
Electrodeposition
Photoabsorption
Areal capacitance
Microstructural

ABSTRACT

Here in, we report electrodeposited Mn_3O_4 thin film doped with various level of Zn dopant ($0 \leq x \leq 5.0, \%$), on a layer of indium tin oxide (ITO) on glass substrate. The deposition route involves the use of two-electrode electrochemical cell system comprising graphite and the substrate as counter and working electrodes, respectively. Some surface properties such as those of morphological, crystal structure, optical, electrical and electrochemical were studied to evaluate the films' potentials in energy conversion and storage devices. Microstructural studies revealed the films grew with isotropic morphology of good tetragonal shaped crystal structure with even distribution and possessing required surface area on the substrate surfaces. Raman prominent peak at 659 cm^{-1} wave number indicates a typical A_{1g} Raman vibrating mode of Mn^{2+} in a Mn_3O_4 spinel structure. The crystallite size and microstrain values were found varying from 38 to 43 nm and 5.6×10^{-3} to 3.2×10^{-3}, with respect to increase in dopant content, respectively. Energy band gap and Urbach energy were varied from 3.28 to 2.68 eV and 1.59 to 2.17 eV with increasing level of dopant content, accordingly. Electrochemical charge storage area capacitance (12.62 to 21.35 mF cm^{-2})/capacity (5.1 to 8.1 μAh cm^{-2}) and rate capability of Mn_3O_4 electrode were found to improve with Zn dopant. The work therefore discusses the tailoring of band absorption and supercapacitive characteristic of electrodeposited Mn_3O_4 thin film with Zn-doping for enhanced energy application.

1. Introduction

Manganese is regarded as a transition metal useful in various applications owing to its broad and unique characteristics which include high heat resistance and ionization energy, high hardness and brittleness, easy oxidization and so on (Greenwood and Earnshaw, 2012). Manganese oxides are among the transition metal oxides with novel functioning properties that have been extensively studied due to the level of redox, morphological and structural characteristics they portray (Greenwood and Earnshaw, 2012; Ghosh, 2020). They are also endowed with the formation of several transition states and as such, the catalytic properties of Mn_xO_y can be traced to the formation of various oxides such as MnO, MnO_2, Mn_2O_3, MnO_3 and Mn_3O_4, and so on, via several oxidation states and oxygen vacancies in their crystal lattices. These oxides have demonstrated excellent optical, structural, catalytic and charge transport performance (Ghosh, 2020). Therefore, they have been shown to possess remarkable potentials for photocatalysis, sensing, batteries and supercapacitor applications. Nanostructured Mn_xO_y possesses improved surface area to volume ratio which have been extensively used towards these applications (Chen et al., 2012). Among these oxides, Manganosite (MnO) takes the form of rock salt mineral oxide. Bixbyite, a trivalent Mn-oxide occurs as either mineral (α-MnO_3) or as thermally less stable one (γ-Mn_2O_3) which is not ubiquitous in nature. MnO_2 (pyrolusite) and Mn_3O_4 (hausmannite) have been found to be the most stable manganese oxides. MnO_2 has been extensively used in the development of energy storage devices such as battery and as electron acceptor through reversible redox process during charging and discharging (Ghosh, 2020). Hausmannite which is the core of this study forms a spinel structure $(Mn^{2+}(Mn^{3+})_2O_4$ with Mn^{3+} and $Mn^{2+})$

* Corresponding author.
E-mail address: adeksaheed007@gmail.com (S.A. Adewinbi).

https://doi.org/10.1016/j.rsurfi.2023.100123
Received 24 October 2022; Received in revised form 3 May 2023; Accepted 18 May 2023

occupying the octahedral and tetrahedral sites, respectively and with closely packed cubic oxide structure and lattice constant (a = b = 0.5762 Å and c = 0.9470 Å). However, only a few reports on the performance of manganese oxide thin film as optoelectronic contacts are available. This has been attributed to a number of difficulties experienced in tailoring its band gaps to suit the demands (Suib, 2008; Ghosh, 2020).

Modulation of the band gap of the semiconductor in use is critical in the fabrication of optoelectronic and charge storage devices. There are two processes involved in this. The first is the quantum confinement approach, which involves varying the particle sizes by changing some depositions conditions that are attached to the growth processes and the incorporation of a foreign atom as a dopant impurity is the second route. The latter entails the substitution of dopant ions for cations in the host lattice. A number of deposition routes for the syntheses of pure and doped Mn_3O_4 thin film have been reported. For example, Bayram and colleagues investigated the morphological and photocatalytic properties of high thermally stable metal-ion-doped and undoped Mn_3O_4 thin films on soda lime glass substrate deposited via an ionic layer reaction and absorption process (Bayram et al., 2018). Similarly, Kocyigit, reported the synthesis of an Au@Mn_3O_4 nanostructured thin film by spray pyrolysis and a reduction in band gap and transmittance was observed (Kocyigit, 2018). The variation in thickness effect on some physicochemical and optical properties of spray pyrolyzed Mn_3O_4 nanostructures has also been investigated by Shano and co-worker (Shano et al., 2021).

Several transition metals have been utilized as dopant impurity atom for potential modulation of optoelectronic and supercapacitive properties of Mn_3O_4 nanostructures (Bayram et al., 2018). Amongst these transition metals, Zn^{2+} was chosen for this study owing to its tetrahedral coordinated 3d orbital singlet ground state, and its ionic radius being approximately the same as that of Mn-ion (Adewinbi et al., 2022a). Furthermore, the introduction of more oxygen vacancy by the Zn dopant could create more absorption sites as a result of its partially filled electronic configuration. As a result, the microstructure, optical and electrical properties of Mn_3O_4 and Zn-doped Mn_3O_4 thin films were thoroughly studied in this study to evaluate its influence in the photocatalytic and photoabsorption characteristics of the host film. The dopant effect on the electrochemical supercapacitive performance of the host film was also part of the investigation. Two-electrode electrochemical deposition system was adopted for this study, thus revealing the uniqueness of this study. The films were grown on conducting ITO precoated on glass substrate. This research focused on the impact of effect of Zn ion dopant on the two electrode-electrodeposited Mn_3O_4 thin film. To our knowledge, this is the first time such a report will surface. We investigated the effect of different Zn-dopant concentrations on the microstructure, electrical properties and optoelectronic band gap modulation of Mn_3O_4 nanostructured thin films using a scalable and inexpensive electrodeposition approach with a view to unveiling its unique properties suitable for enhanced optoelectronic and supercapacitive performance. Electrodeposition has been a unique way of producing various nanostructured compound for several applications (Taleatu et al., 2018; Adewinbi et al., 2020, 2021a,b, 2022a) . It is suitable for achieving tunning and replacing some Mn^{2+} with Zn^{2+} ions in the solution growth process to modulate its lattice states and enhance conductivity through the tailoring of its energy band gap. Interestingly reports have presented the absorption properties of some transition metal ions including Mn^{2+} in solutions, thus revealing its potentials for electrodeposition of its semiconducting material (Ibrahim et al., 2021; Adewinbi et al., 2022b; Ali et al., 2022; Ibrahim et al., 2022; Mohamed et al., 2022). There are many advantages associated with these methods. They include simplicity and cost effectiveness, variable deposition conditions including deposition period, solution concentration and deposition voltages, among others (Taleatu et al., 2018; Adewinbi et al., 2022a).

2. Materials and method

2.1. Raw materials

The materials involved in this study encompasses high purity chemical reagents (99%, Sigma Aldrich): manganese sulphate hexahydrate, zinc sulphate hexahydrate; Potassium hydroxide pellets and conductive indium tin oxide coated glass substrate (ITO/glass; from lumtech inc, China) of surface resistivity 15 Ω/m^{-2}, dimension: 1.5 × 1.0 x 0.1 cm.

2.2. Electrolytic solution and films' preparation

For the preparation of the electrolytes, 0.05M manganese sulphate host solution ($MnSO_4$(aq)) was prepared by dissolving 1.6902 g of manganese sulphate monohydrate in 200 ml of deionized water and spinning the mixtures using a magnetic stirrer to obtain homogeneous solution. 0.1M KOH solution was also prepared from the dissolution of a certain mass of KOH in 200 mL of deionized water while $ZnSO_4$ dopant electrolyte was prepared by dissolving its corresponding salt in the same vein as the dopant solution. Electrolytic solutions 1 and 2 were separately prepared from the addition of droplets of 0.01M KOH solution separately to the prepared $MnSO_{4(aq)}$ and $ZnSO_{4(aq)}$, respectively. The experiment also involved the use of a substrate composed of a layer of conductive indium doped tin oxide (ITO) film precoated on glass. The ITO/glass was washed and cleaned thoroughly with deionized water, ethanol and acetone sequentially and ultrasonically for a few hours to remove oily substance or any other suspected surface impurity from handling.

Pure Mn_3O_4 and Zn (1%–5%) doped Mn_3O_4 thin film samples were grown separately and directly on the cleaned ITO substrate from the prepared electrolytes, accordingly and using a home made two-electrode electrodepositing cell system at ambient temperature (see Figure Scheme 1). The cell system set-up encompasses glassy carbon (graphite) and the ITO/glass substrate as the counter and working electrodes, respectively and coupled with a digital multi-meter and a dc power supply unit. Growth of bare Mn_3O_4 thin film (sample M1) was established by pouring electrolytic solution 1 into the cell, and appropriate connections were made in accordance to reports in some of our previous works (Taleatu et al., 2018; Adewinbi et al., 2020, 2021a,b, 2022a). The anodic growth was established with growth voltage and deposition time of 2.2 V and 10 min, respectively. After the growths, the as-deposited sample was taken out of the cell, rinsed with distilled water and oven dried at 130 °C to get rid of the remaining surface water content. After drying all the samples, they were selected for annealing in a furnace at temperature of 350 °C for 1hr. This was with a view to ensuring optimum crystallinity of the films' grains. The annealing process will also orient the film particles and ensure they are well positioned into their proper equilibrium spots. In the same vein, the doped samples (samples ZM2, ZM3 and ZM4) were obtained from the mixture of electrolytic solutions 1 and 2, with solution 2 occupying 1%–5% of the entire volume as tabulated in Table 1.

2.3. Material characterization

The pure and doped Mn_3O_4/ITO thin films on glass were characterized with the aid of some under-listed microstructural, optical and electrical probing techniques. Surface morphological studies of the samples were characterized using field emission scanning electron microscope (Carl Zeiss Ultra plus 55, Oberkochen, Germany) (FESEM) which was coupled with energy dispersive X-ray spectroscopy (EDX) for samples elemental components' identification. XPER-PRO BV analytical powdered X-ray diffractometer of CoK α-radiation of λ = 1.78901 Å. A Witec alpha 300 RAS + confocal micro-Raman microscope was employed to obtain Raman data at laser and power excitation wavelengths 2 mW and 532 nm, respectively and acquisition period 120 s. The

Table 1
Electrolytic conditions for the growth and structural parameters of doped and Zn-doped Mn_3O_4 thin films.

S/n	Film samples	Electrolytic condition		Grain size, D (nm)	Microstrain, ϵ (eV)	Dislocation density, $\delta \times 10^{14}$ (lines/m^2)
		Solution I (%)	Solution II (%)			
1.	M1	100	0	38.19	0.0056	6.856
2.	ZM1	99	1	39.12	0.0037	6.534
3.	ZM2	97	3	40.13	0.0035	6.210
4.	ZM3	95	5	42.98	0.0032	5.413

samples were also probed electrically using sheet resistance measurement from a kelvin probe (Four-point). The probes were positioned at equidistance and collinearly on the film such that the currents are measured via the two outer probes while the voltages were applied through other two probes at the inner side. The voltage and current leads were separated to avoid error emanating from the electrical contacts. Optical measurements were taken from the absorbance and transmittance data of the samples obtained from a double beam BK-UV 1900 PC Ultraviolet–visible (UV–Visible) spectrophotometer between the spectra wavelength ranging from 200 to 900 nm at normal incidence and ambient temperature. Electrochemical properties unveiling supercapacitive performance of the fabricated electrodes from the prepared films were investigated using the procedure previously reported in one of our previous works (Adewinbi et al., 2021b).

3. Results and discussions

3.1. Surface microstructure and elemental studies

The surface morphological micrograph images of the deposited undoped and doped Mn_3O_4 thin film samples are shown in Fig. 1(a–d) as determined by FESEM. The micrographs generally show that the films have good adherence to the ITO/glass substrates. For the undoped Mn_3O_4 film (Fig. 1(a)), random and irregular shaped particles with varying sizes were found formed and distributed across the surface of the substrate. This surface morphology was observed to improve as the dopant concentration increased. Isotropic and uniform nano-shaped crystals lacking aggregation were observed with even distribution in the micrographs of the doped samples. These observable features also seem to be more obvious in the at higher dopant concentration. Average pore size of the Mn_3O_4 film also reduced with increasing Zn-dopant content. These enriched features as observed from the SEM images of the doped samples indicate the influence of the dopant ion on the microstructural properties of the deposited film and can be attributed to homogeneous nucleation and assembly of the Mn_3O_4 thin film crystals covering the ITO substrate by Zn atom in the solution during the electrodeposition procedures (Xu et al., 2006). The uniform and evenly distributed grains as observed in doped samples revealed enhanced surface area that can give optimum reactive sites and continuous pathway for effective charge transitions and enhance photoabsorption through maximum light scattering, when used as photoanode in optoelectronic devices (Dubal et al., 2010). The images were also processed using microscopic image processing software package (image J) and the result reveals particle sizes of the deposited films are with nanometer ranges.

The elemental composition of the deposited undoped and Zn doped Mn_3O_4 thin film on ITO substrate were examined using EDX spectra given in Fig. 2. As expected, the spectrum belonging to pure Mn_3O_4 film sample reveal Mn and O signals including some element emanating from the substrate properties (Fig. 2(a)). In addition, the spectrum of the Zn-doped Mn_3O_4 thin film also reveal signals of O, Mn and Zn elements (Fig. 2(b)). Absence of signals from any impurity elements shows that the deposited structures are of high purity. The distribution of this elements as revealed from the Zn-doped Mn_3O_4 films grains was investigated with the aid of EDX elemental map images captured at higher magnification. These maps depict position of each element and are presented in Fig. 3(a–f). From the maps, it is revealed that all these characteristic elements are evenly positioned across the films' grains. The feature also shows that there was no formation of Zn-dopant separate oxide indicating that the Zn dopant impurity was well incorporated within the host (Mn_3O_4) grain lattice.

3.2. Crystal structure and raman studies

The XRD patterns of both undoped Mn_3O_4 and Zn-doped Mn_3O_4 thin films deposited on conductive FTO glass substrate are shown in Fig. 4(a). The Fig. depicts the plots of diffraction intensity against position angle 2θ ranging from 20° to 70° after background noise had been subtracted within the diffraction angle. Several diffraction peaks were displayed from the XRD spectra indicating Bragg's law of diffraction has been satisfied and reaffirms the deposited films are composed of crystalline particles as depicted from the FESEM micrographs (Adewinbi et al., 2022a). The most prominent characteristic peaks sighted at (112) plane as presented by the XRD patterns of the undoped and Zn-doped Mn_3O_4 samples were observed to match well with those for a single phase Mn_3O_4 tetragonal crystal structure. These diffraction peaks formed from reflection of (hkl) indices (112), (211), (105), (312), (303), (224), (103), (200) and (400) observed at their respective position of 2θ can be traced to reference code (JCPDS PDF 01-080-0382; space group 14_1 lamd) (Bayram et al., 2018). There exist no other peaks which can be attributed to the formation of ZnO nanoparticle of some other impurity compounds except those traceable to ITO substrate on the XRD pattern. This thus suggests that the deposited undoped and Zn-doped Mn_3O_4 thin films are highly crystalline and Zn ion was well incorporated into the Mn_3O_4 crystal lattice. Similar results have also been reported in literature (Jha et al., 2012; Bayram et al., 2018). The crystallinity of Mn_3O_4 thin films was found to improve with zinc dopant concentration since the intensities of its characteristic peaks increased with the dopant content. Comparing the patterns of the deposited films, the position angle 2θ of each peak was also observed to shift slightly to higher angle with as the Zn dopant concentration increased. The increment may be due to the rearrangement of microstructure of Mn_3O_4 structure as Zn ion was incorporated due to the ionic radius difference between Zn^{2+} (0.74 Å) and Mn^{2+} (0.80 Å) which may lead to uneven substitution of zinc ion into the Mn_3O_4 crystal matrix. The shift in the position of 2θ may as well be attributed to crystal defect or stress within Mn_3O_4 structure because of addition of Zn atoms to the lattice structure. The significant transformation in crystal structure such as broadening and narrowing of the peaks' width and length of the XRD pattern is often caused by crystal stress or defect (Owoeye et al., 2019, 2021). The formula for calculating a tetragonal crystal structure's lattice parameters is given in Equation A (Bayram et al., 2018; Adewinbi et al., 2021a). The values of the lattice parameters (a and c) for the samples from the preferred growth orientation plane (112) are shown in Table 1. By constraining the lattice parameter c to zero, Laue indices, or the (hk0) plane, were taken into consideration to obtain the lattice parameter a. The values of the samples' interplanar distance (d), also known as the reciprocal lattice vector's length (hkl), were determined using equation B (where hkl are miller indices). Lattice parameter (c) from the preferred growth orientation plane (112) was obtained by substituting the evaluated value of lattice parameter (a) into equation A. It was found that the zinc content slightly reduced the lattice parameters of Mn_3O_4. The

Scheme 1. Schematic representation of the two-electrode electrodeposition process of the growth of Zn-doped Mn_3O_4.

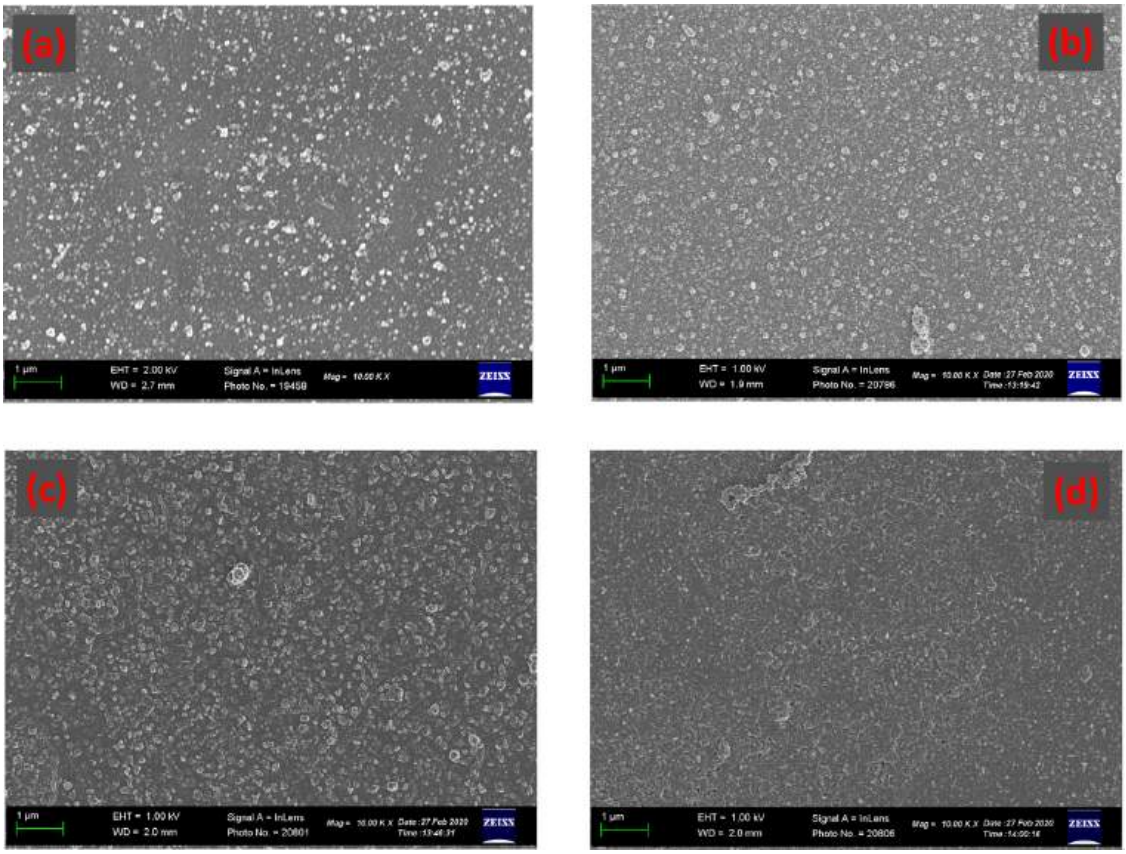

Fig. 1. FESEM micrograph of (a) pure (undoped) Mn_3O_4/ITO film (b) 1% Zn doped Mn_3O_4/ITO film (c) 3% Zn doped Mn_3O_4/ITO film (d) 5% Zn doped Mn_3O_4/ITO film.

difference in ionic radius between zinc and manganese may account for the variation in the lattice parameter of Mn_3O_4 with increased Zn^{2+} content (Kim and Park, 2004; Jha et al., 2012). Increased zinc doping of Mn_3O_4 may have caused a crystallographic defect and a lattice mismatch that resulted from interactions between the host particles and the dopant [9]. The variation in the Mn_3O_4 c/a ratio with increased zinc content was due to the valence electron difference between zinc and manganese ions which further confirms the successful substitution of zinc ions into Mn_3O_4 crystal lattice (Ran et al., 2013; Larbi et al., 2015).

Consequently, Williamson Hall model which modified the commonly known Scherer's formulae, illustrated in relation in Eq. (1) was employed to estimate microstrains (ε) and average grain sizes (D) of the deposited films.

$$\frac{1}{d^2} = \frac{h^2 + k^2}{a^2} + \frac{l^2}{c^2} \quad \text{(A)}$$

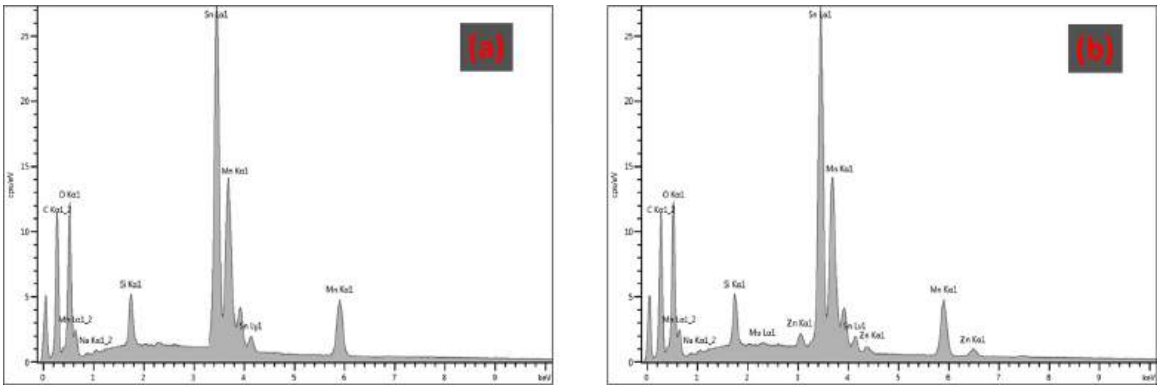

Fig. 2. EDX spectra of the deposited undoped and Zn-doped Mn_3O_4/ITO thin films.

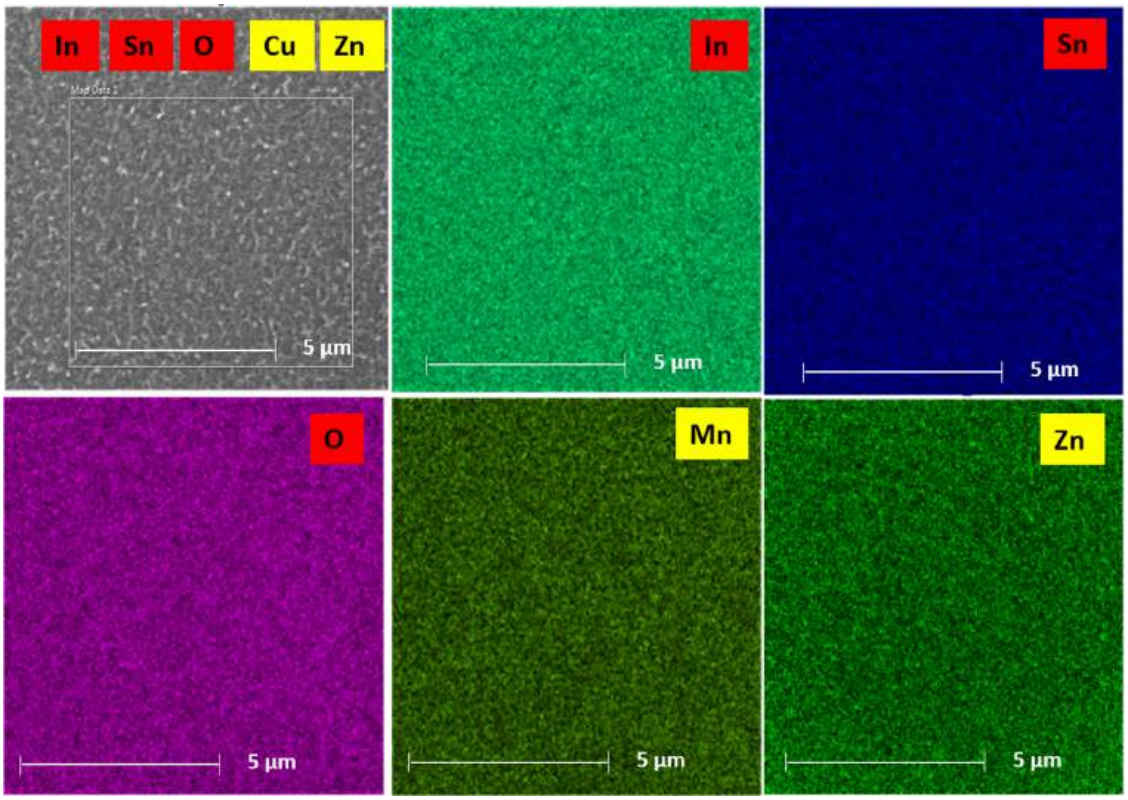

Fig. 3. EDX elemental map images for the deposited Zn-doped Mn_3O_4/ITO thin film.

$$d = \frac{n\lambda}{2sin\theta} \quad \text{(B)}$$

$$\beta = \frac{0.94\lambda}{Dcos\theta} + 4\varepsilon tan\theta \quad (1)$$

Where β, λ, and θ represent peak's full width at half maximum, wavelength of the X-ray, and diffracting angle, respectively. The model plotted the data obtained $\beta\cos\theta/\lambda$ against those for $\sin\theta/\lambda$, and for the intercept and slope of the plot were used to estimate the average grain sizes of the films and average microstrain induced in the grain crystals, accordingly. These plots are shown in Fig. 4(b). Subsequently, dislocation density (δ) of each film was also calculated using the relation: $\delta = \frac{1}{D^2}$. The estimated values of these parameters are presented in Table 1, accordingly. The values of grain size and microstrain were plotted against the dopant contents for each film sample (Fig. 4(c)). The average grain size of the Mn_3O_4 thin film was observed to increase with increasing Zn-dopant. The microstrain on the other hand was observed to slightly decrease with increased dopant concentration. This result shows that grain size is inversely proportional to microstrain and that the increase in the grain size of Mn_3O_4 with increased zinc dopant is an indication of reduction in microstrain and dislocation in the film's particles. The variation in the strain values can be traced to vibrational differences from annealing effect on the samples as a result of varying thermal properties of the substrates and films' particles. This consequently resulted in enhancement of diffusion of Zn ion into Mn_3O_4 crystal lattice thereby forming larger crystallite and improving the overall crystal structure. The agglomeration of crystal to form more single crystals with a reduction in deformation might also likely result in reduction of the strain values and consequently, the dislocation density (Ristić et al., 2013; Owoeye et al., 2022).

The identification of various oxide in samples through a change in polarization has been achieved by Raman spectroscopy. It can also be used to corroborate the findings from the crystal structure characteristic evaluated by XRD analysis. The Raman spectroscopy analysis as shown in Fig. 5 was carried out within the spectral range of 200–1400 cm^{-1} while the inset shows the graph of FWHM for the most prominent peak on the Raman spectra against the dopant concentration. From the

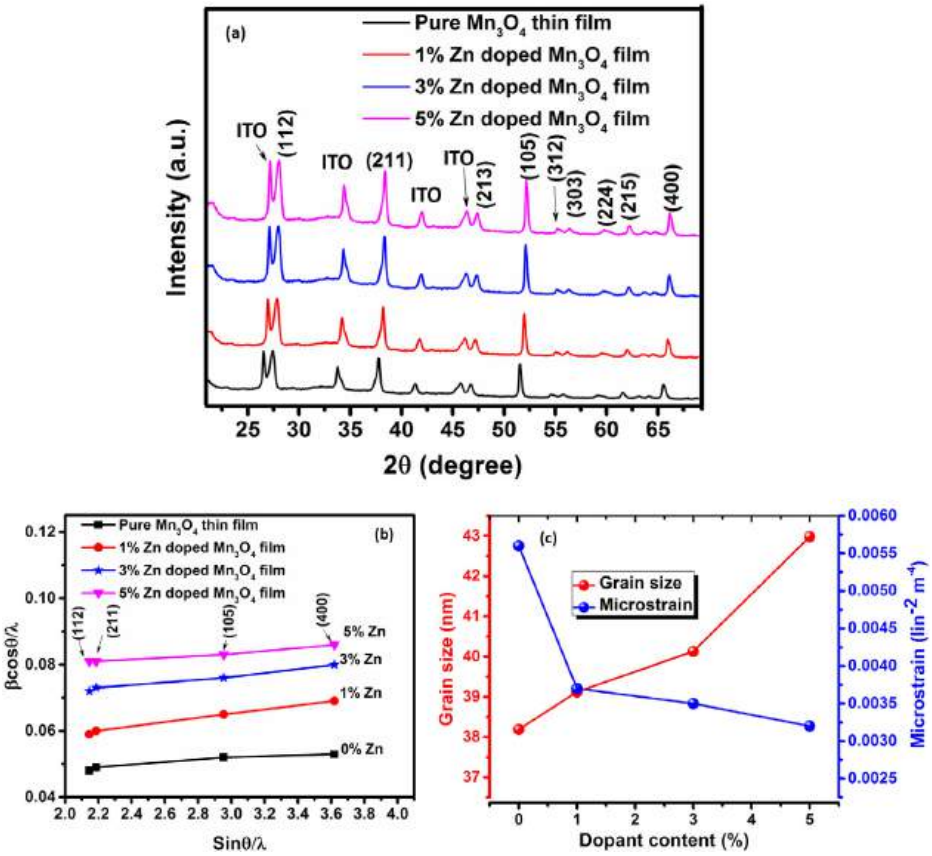

Fig. 4. (a) XRD patterns of the deposited undoped and Zn-doped Mn_3O_4/ITO thin films (b) Williamson Hall plots for estimation of grain sizes and microstrain (c) Plots of grain size and microstrain against dopant contents for the deposited Mn_3O_4/FTO films.

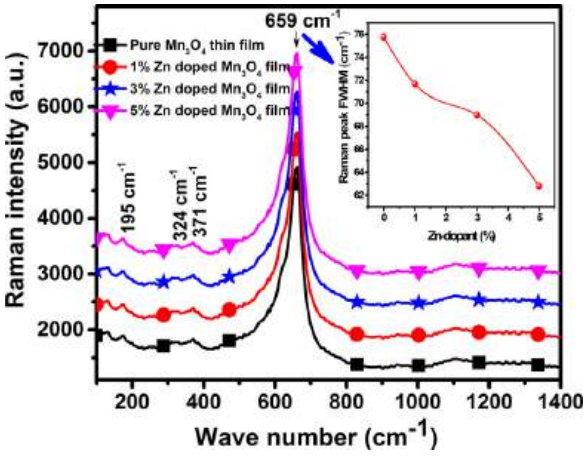

Fig. 5. Raman spectra of the deposited undoped and Zn-doped Mn_3O_4/ITO thin films (inset: plot of FWHM of the peak centered around 659 cm^{-1} wave number).

Raman spectra, three weak peaks are observed at 195 cm^{-1}, 324 cm^{-1} and 371 cm^{-1} while a strong and intense peak is observed at 659 cm^{-1}. These peaks are in agreement with the Raman spectra of Mn_3O_4 (Dubal et al., 2010; Ristić et al., 2013; Bayram et al., 2018) and the absence of any other peak exclude the presence of other oxides of manganese. The peak intensity of Zn-doped Mn_3O_4 occurring at 659 cm^{-1} increased with dopant concentration and showed that an increase in the doping concentration of Zn resulted in broadening and increased intensity of the peaks with the 5% Zn-doped Mn_3O_4 film sample typifying the most intense and broad peak. In a report by Xu et al. (1999), increase in Raman peaks intensities is an indication of increasing grain size of nanoparticles. The observed increase in intensity of Raman peaks of the deposited Mn_3O_4 particles with Zn dopant can be ascribed to the local optical vibration of Zn atom within Mn_3O_4 crystal lattice, led to increasing crystal sizes and thus corroborate the observable features obtained from the XRD studies. The peak at 659 cm^{-1} is typical of all spinel structures (Kocyigit, 2018) and is correlated to the A_{1g} mode of Mn^{2+} ions in Mn–O vibrational mode (Bayram et al., 2018; Ghosh, 2020) while the peaks at 371 cm^{-1} and 324 cm^{-1} are symbolic of the T_{2g} and E_g active Raman modes of Hausmannite tetragonal crystal structure, respectively corresponding to bending mode Mn–O with non-symmetric bridged oxygen species (Mn–O–Mn) (Xu et al., 1999; Ristić et al., 2013; Bayram et al., 2018). The FWHM showed a decrease from 76 cm^{-1} to 62 cm^{-1} as the Zn dopant increased from 0% to

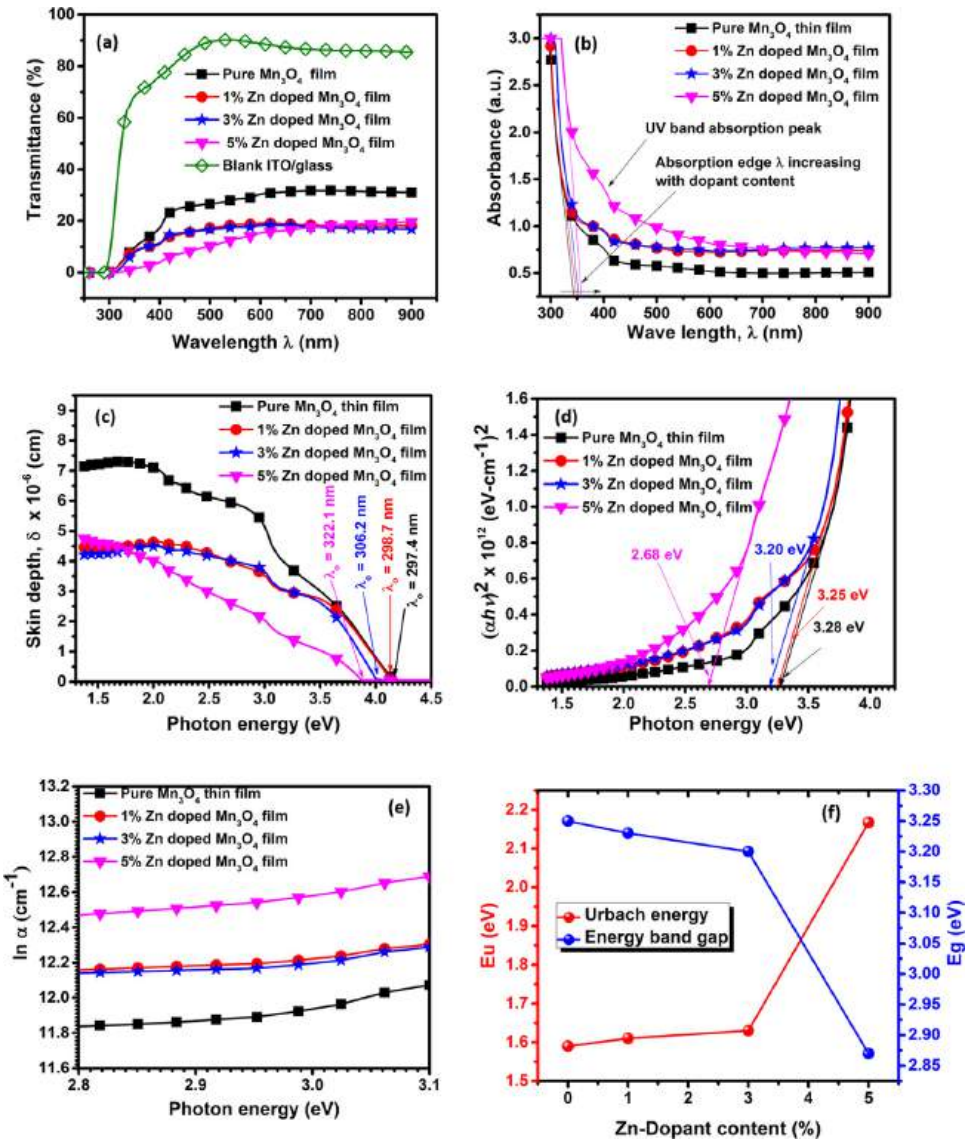

Fig. 6. (a and b) Films' UV–Vis optical transmittance and absorption spectra (c) Optical skin depth plots against spectra wavelength (d) Tauc's plots for estimations of Films' energy band gaps and (e) plot of ln α against the energy of photon for the deposited films for estimations of Urbach energies content and (f) plots of estimated energy band gap and Urbach energies as function of Zn dopant content for the deposited undoped and Zn-doped Mn_3O_4/ITO thin films.

5%. This may be due to the fact that the ionic radius of Mn^{2+} is larger than the ionic radius of Zn^{2+} (Jha et al., 2012). This shows that there is remarkable crystallization of the Mn_3O_4 film as the doping concentration increased and thus reaffirmed an increase in the grain size as the Zn doping concentration increased as depicted in Fig. 4(c) (Adewinbi et al., 2022a)

3.3. Optical studies

Fig. 6(a–f) shows the analysis of the UV–Visible data obtained from the optical spectrophotometer. Firstly, as observed from the transmittance spectra (Fig. 6(a)), one could see that the deposited films are not significantly transparent to visible light when compared to the highly transmitting ITO coated glass substrate. This also exemplifies high photoabsorption capability of the deposited structures. It is also obvious from the spectra that introduction of Zn ions into the matrix of Mn_3O_4 led to increased absorption of the light photons which is capable of increasing the carrier concentration of the doped Mn_3O_4 thin films. Though little variations in transmittance were observed in the 1% and 3% doped Mn_3O_4 samples, 5% doped Mn_3O_4 shows remarkable reduction in transmittance and consequently could possess better carrier generation rate as a result of the increased Zn^{2+} shallow donors in the bandgap (Adewinbi et al., 2020; Ghosh, 2020).

These observations were corroborated by the red-shifting of the absorption edges of the samples with increasing Zn^{2+} dopant concentrations as shown in Fig. 6(b). Expectedly, 5% doped sample exhibited the highest absorbance and red-shifted far into the visible region of the electromagnetic spectrum. This further confirms the band-bending effects of Zn^{2+} dopant in the Mn_3O_4 films. More importantly, it shows the absorption behavior and as such band structures of the Mn_3O_4 could be modulated by adjusting the concentration of its dopants (Adewinbi et al., 2021a, 2022a)

These variations in composition occasioned by inclusion of dopant atoms in Mn_3O_4 films are capable of instituting changes in their textural properties, optical density and surface microstructures. One of such parameters that reflect these changes is the skin depth δ. It is a measure of the depth to which electromagnetic radiation can penetrate a film surface as their oscillation frequency increases. It has an inverse relationship with the absorption coefficient α given by Eq. (2) (Adewinbi et al., 2021b,c, 2022a).

$$\delta = \frac{1}{\propto} \tag{2}$$

Table 2
Optical energy band and electrical parameters of the deposited doped and Zn-doped Mn_3O_4 thin films.

S/n	Film samples	Energy band gap, Eg (eV)	Band tail width, Eu (eV)	Resistivity, $\rho \times 10^{-4}$ (Ω m)	Sheet resistance, R_{sh} $\times 10^4$ (Ω)	Conductivity, σ $\times 10^3$ (Ω m)$^{-1}$
5.	M1	3.25	1.59	3.760	1.209	2.660
6.	ZM1	3.23	1.61	2.740	0.975	3.650
7.	ZM2	3.2	1.63	1.760	0.638	5.681
8.	ZM3	2.87	2.167	1.430	0.426	6.993

Where α is also given by Eq. (3) assuming negligible reflection,

$$\alpha = \frac{1}{t} ln(T) \tag{3}$$

Where T is the normalized transmittance data and t represents the thickness of the film in nm. The plots of δ against photon energy for all the films are depicted in Fig. 6(c). It can be seen that the films exhibit different cut-off energy and wavelengths which varies directly with the amount of dopant concentrations. Beyond the cut-off wavelength of a thin film, the absorption process ceased and penetration of light photons of higher wavelength proceeds (Taleatu et al., 2018; Adewinbi et al., 2021c). Interestingly, 5% doped sample exhibits the longest cut-off wavelength of 322 nm. This confirms its transmittance and absorption behaviors shown in Fig. 6(a and b). More importantly, it shows that increase in Zn^{2+} dopant concentration has corresponding impact on the textural and optical properties of the Mn_3O_4 film.

The optical band gaps of all the films were estimated by exploring the relationship between the photon energy ($h\nu$) of the incident light and the absorption coefficient using the Tauc's model according to the relation in Eq. (4) below (Adewinbi et al., 2021d).

$$(\alpha h\nu)^{1/n} = \aleph \left(h\nu - E_g\right) \tag{4}$$

Where $\aleph$, E_g and n indicate the band tail constant, energy band gap, and optical transition mode (2.0/0.5 for indirect/direct allowed transition), respectively. The linear portion of the plots (α^2vs. $h\nu$) were extrapolated to a point where $\alpha^2 = 0$ (Fig. 6(d)) *to* estimate energy band gap. The films generally exhibit direct band transition with relatively wide band gaps. This gap is due to the attenuation resulting from separation between the valance and conduction band of the semiconductor (Ghosh, 2020). The band gap values of the films reduced from 3.28 to 2.68 eV with increasing Zn^{2+} dopant concentration as presented in Table 2 and 5% doped sample showed the highest band narrowing as expected owing to its formation of more localized states as a result of huge increase in dopant ions (Adewinbi et al., 2022a). The reduction in these values corroborates the enhanced photoabsorption characteristics observed in the transmittance spectra with increasing Zn-dopant. In addition, the undoped Mn_3O_4 exhibits the widest band gap confirming that the observed band narrowing was a result of the Zn ion dopants. This observed difference in band-gap values corroborates the absorption pattern of the films. Similar results on effect of Zn ion dopants on band structure have been reported (Bayram et al., 2018; Adewinbi et al., 2022a).

The optical bandgap gives basic insight into the band-to-band transition properties of semiconducting materials. However, lattice distortions or disorder occasioned by defects such as dopant ions are capable of producing extended localized states in the energy gap of such materials even beyond the lower limit value of the bandgap, thus leading to formation of localized states energy commonly called Urbach energy (band tail width, E_u) (Taleatu et al., 2018; Busari et al., 2020; Adewinbi et al., 2021c, 2022a). Hence, it is a measure of contribution of these localized states to absorption properties of the semiconductor (Adewinbi et al., 2021c, 2022a). The Urbach energy of the films was calculated according to the Eq. (5), where $\alpha_o$andE_c are material constants, E is the photon energy and E_u denotes the width of the tail of localized states (Larbi et al., 2015; Taleatu et al., 2018).

$$\propto (E) = \alpha_o exp\left(\frac{E - E_c}{E_u}\right) \tag{5}$$

The inverse of the slope of the linear fit obtained from the plot of ln (α) against the photon energy, E gives the Urbach energy, E_u after linearization. The plots are shown in Fig. 6(e). The calculated values of E_u are presented in Table 2. Plots of energy band gap and Urbach energy values for the grown structures against dopant content are depicted in Fig. 6(f). The plots show the E_u increases with increasing dopant concentration and more importantly, 5% doped sample showed highest value across all photon energy values. However, bang gap value reduced as the dopant content increases. It is then not out of place to conclude that the increased absorption of photons and band narrowing observed in Zn-doped samples are associated to the introduction of defect and formation of localized states by dopant ions in the band structure of Mn_3O_4.

3.4. Electrical characterization

The electrical properties of the deposited pure and Zn-doped Mn_3O_4 films explored from the Four-point probing were examined using the measured current plots against the applied voltage data. The plots are shown in Fig. 7(a). Ohmic response of the films observed curves as the currents increased linearly with the applied voltages (Taleatu et al., 2018; Adewinbi et al., 2021d). It can also be observed from the plots that the current response of Mn_3O_4 film increases with respect to Zn-content, implying high possibility of possessing improved electrical conductivity and deteriorating electrical resistivity as the dopant concentration increases. The electrical resistivity (ρ) was deduced using the relation in Eq. (6), and consequently, the electrical conductivity (σ) and sheet resistance (R_{sh}) were calculated using Eqs. (7) and (8), accordingly (Taleatu et al., 2018; Adewinbi et al., 2020). The results are tabulated in Table 2.

$$\rho = \left(\frac{V}{I}\right) \times 2\pi s \tag{6}$$

$$\sigma = \frac{1}{\rho} \tag{7}$$

$$R_{sh} = \frac{\rho}{d} \tag{8}$$

Where V, I, s and d, are the potential applied (in mV), current measured (in mA), probe spacing (1.5 mm) and the film's thickness (in nm). Fig. 7(b) depicts the relationship that exist between the calculated conductivity and sheet resistance of Mn_3O_4 thin film with Zn-dopant content. The plots show the deposited Mn_3O_4 thin film on ITO wherein the electrical conductivity increased while the sheet resistance decreased as the dopant content increased. This shows that as the dopant content increases, the electron collision with film's surface is enhanced (Panta and Subedi, 2012). The feature can be attributed to the quantum confinement effect which exemplifies those changes in the surface electrical properties of Mn_3O_4 film as a result of the induced pressure and band-gap tunning as observed from the XRD and optical studies, respectively.

3.5. Electrochemical studies

Electrochemical characterizations of the pristine Mn_3O_4 and Zn^{2+} doped Mn_3O_4 thin film electrodes were carried out to study the effect of Zn^{2+} dopants on the electrochemical performance metrics of Mn_3O_4 and in addition, the mass and charge transport associated with their electrochemical cycling were also elucidated. To begin with, the storage

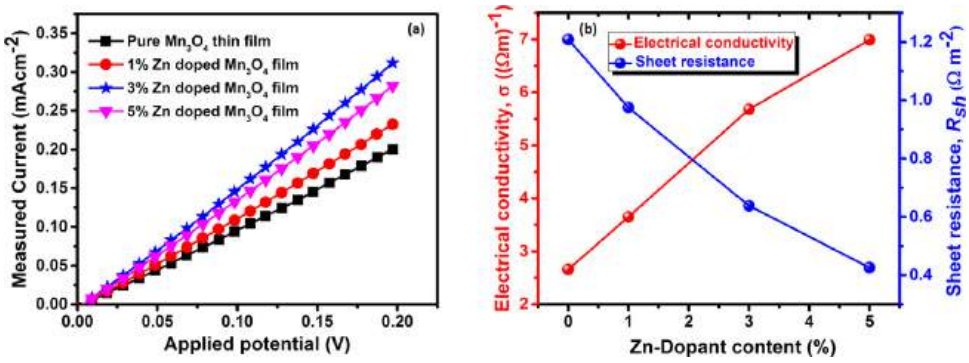

Fig. 7. Electric I–V characteristic curve for the deposited undoped and Zn-doped Mn_3O_4/ITO thin films.

mechanisms of the two sample electrodes (Mn_3O_4 and optimum Zn–Mn_3O_4) were unraveled through cyclic voltammetry measurements in aqueous alkaline electrolyte (1 M KOH) within the voltage window of 0 to 0.6 V (vs Ag/AgCl reference). Fig. 8(a) depicts the cyclic voltammogram taken at the scan rate of 5 mV/s. Both the undoped Mn_3O_4 and the doped Zn–Mn_3O_4 electrodes show near-rectangular CV profiles which is a popular pseudocapacitive storage signature. More importantly, Zn-doped Mn_3O_4 obviously exhibited higher current response which could be connected to the narrower bandgap and improved conductivity earlier indicated by the optical bandgap and I–V characteristics analysis. The surface area of the CV curve is a measure of the charge storage capability of an electrode. Thus, the increased current response and wider surface area of the CV curve of Zn-Mn_3O_4 sample is a clear indication of its superior storage capacity (Ahmed and Nabi, 2021; Adewinbi et al., 2023). Afterwards, the Zn-Mn_3O_4 electrode was cycled at different scan rates from 5 mV/s to 100 mV/s. Fig. 8(b) depicts the CV plots for this optimally Zn-doped Mn_3O_4 electrode at different scan rates. The progressive increment in current response with increasing scan rate is a further confirmation of its pseudocapacitive properties (Adewinbi et al., 2021b). Our estimation of the areal capacitance C_a at different scan rates (S_r) was done by integrating the CV curves with the aid of relation in Eq. (9), where *A, I, V,* represent the area of the active electrode film, applied current and potential range, respectively. The result indicates that Zn-Mn_3O_4 possesses highest areal capacitance of 21.34 mF/cm^2 at the scan rate of 5 mV/s as shown in Fig. 8(c).

$$C_a = \frac{1}{AS_r.V}\int_{v_i}^{v_f} I dV_s \quad (\text{mF cm}^{-2}) \tag{9}$$

The noticeable decrease in areal capacitance with increasing scan rate is linked to the inability of the K^+ to penetrate inner pores of the electrode due to time constraint at higher rates (Nwanya et al., 2017; Adewinbi et al., 2021b). Similar observations have been reported for different pseudocapacitive electrodes (Nwanya et al., 2017; Ponnar et al., 2020; Ahmed and Nabi, 2021; Adewinbi et al., 2022c, 2023). The total charge stored is a combination of the charge transfer process occurring on the surface and in the tunnel of the electrode. Therefore, the loss of contribution from the tunnels resulted in the observed decrease in capacitance at higher scan rates.

Further analysis of the energy storage properties of the electrodes were performed via constant current charge–discharge (CD) testing under the same experimental conditions as stated for the cyclic voltammetry measurement. Typically, charge–discharge profiles of the two electrodes are compared in Fig. 8(d). The CD plot also indicates the pseudocapacitive nature of this electrode with its imperfect triangular-shape profile in complete agreement with the CV analysis. The similarity in the shape of the CD plot also confirms that the electrochemical storage mechanism of the two electrodes is similar. However, the Zn doped electrode exhibits longer discharge time which is a confirmation of its higher storage capacity. The Zn–Mn_3O_4 exhibited an improved capacity of 8.1 μAh-cm^{-2} at discharge current of 5 mA-cm^{-2} compared to the 5.5 μAh-cm^{-2} displayed by the undoped sample electrode which were estimated using Eq. (9) with t representing discharge time (Adewinbi et al., 2022c)

$$Q_a = \frac{\text{I} \times t}{3.6 \times A}(\mu\text{Ah cm}^{-2}) \tag{10}$$

The long-term stability of active electrode materials under cycling is of economic importance to the energy storage community. Thus, we have measured the long-term capacity retention of the two sample electrodes over 2000 charge–discharge cycles. Fig. 8(e) depict the plot of areal capacity against number of cycles. Both electrodes retain over 80 percent of their capacity after 2000 cycles. The initial drop of their capacity over the first three hundred cycles could be attributed to the dissolution of the loosely bounded grains of the active materials into the electrolyte solution. Thereafter, the areal capacity became relatively stable throughout the cycling measurement. The high areal capacitance and good stability of the doped electrodes indicate enhanced suitability for fabrication of high-performance supercapacitors with excellent rate capability. Specifically, the two electrodes exhibit strong CV response in the positive potential region indicating their better suitability as cathodes for fabrication of asymmetric supercapacitors. More importantly, our analysis has shown that doping of the Mn_3O_4 with Zn led to improved electrochemical energy storage performances.

Electrochemical impedance spectroscopic (EIS) testing of the two selected electrodes were carried out within the frequency range of 0.01 to 10^5 Hz. The EIS measurement is capable of elucidating the interfacial interaction between the electrode and electrolyte in an electrochemical testing. Fig. 8(f) is the plot of imaginary component of the impedance against the real component (Nyquist plot). The Nyquist plot could be demarcated into three different regions representing the solution resistance, charge-transfer resistance and Warburg impedance. The solution resistance is estimated from the first point of intersection of the plot on the real axis at the high frequency region. It represents the combined resistance offered to charge transport by the current collector, active electrode material and the electrolyte. The charge transfer resistance is depicted by the depressed semicircle in the medium frequency region of the plot and finally the inclined straight line at the low frequency region represents the Warburg impedance which is a measure of the rate of ionic diffusion in and out of the pores of the active electrode material (Nwanya et al., 2017; Chaudhary et al., 2021; Sim et al., 2021; Adewinbi et al., 2022c). Obviously, the Nyquist plot shows that the Zn doped electrode exhibit slightly lower impedance values compared to the undoped Mn_3O_4 in close agreement to the earlier observed narrower band gap of the Zn-doped Mn_3O_4. Furthermore, the slope of the inclined straight line suggests faster ionic diffusion rate in Zn-Mn_3O_4. This could be attributed to structural variations occasioned by the presence of Zn interstitial in the matrix of Mn_3O_4 and perhaps, the adjustment of the surface electronic structure of Mn_3O_4 due to the presence of Zn^{2+} dopants.

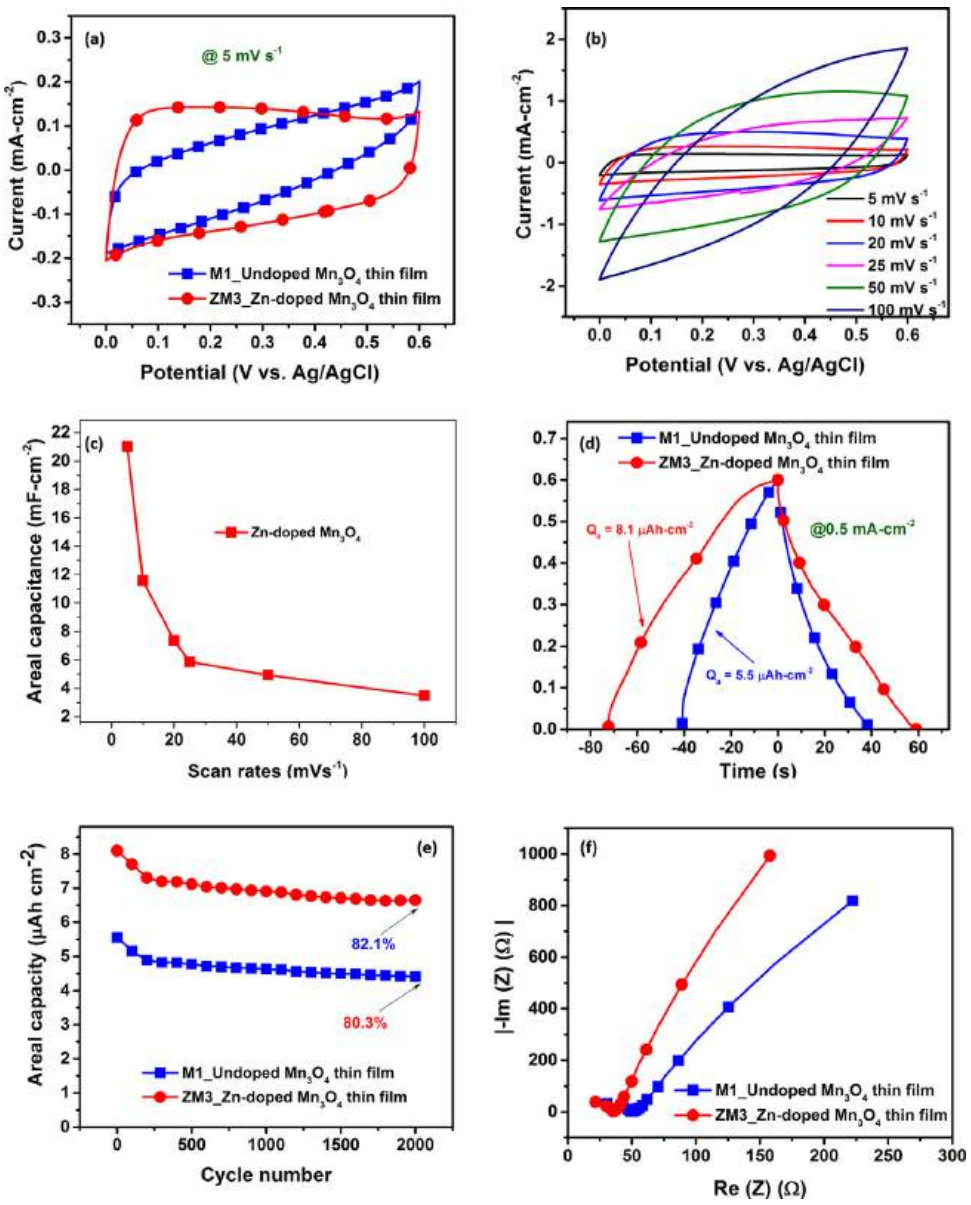

Fig. 8. (a) CV curves of undoped and Zn-doped Mn_3O_4 thin film electrodes at 5 mV s^{-1} scan rate (b) CV curves of Zn-doped Mn_3O_4 thin film electrode at scan rate range 5–100 mV s^{-1} (c) plot of calculated areal capacitance of Zn-doped Mn_3O_4 thin film electrode vs. scan rate (d) CD curves of undoped and Zn-doped Mn_3O_4 thin film electrodes at 0.5 $mAcm^{-2}$ current density (e) plot of areal capacitance vs. number of cycles as a measure of stability (f) EIS Nyquist plots for the undoped and Zn-doped Mn_3O_4 thin film electrodes.

4. Conclusion

In this report, a two-electrode electrodeposition system was employed to prepare various level of Zn-doped Mn_3O_4 thin films on conductive Indium tin oxide coated on glass. All the films samples were heat treated at temperature of 350 °C. Some surface microstructural, optical and electrical characterization were carried out to examine the film's potential for optoelectronic application. Morphological studies showed isotropic and uniform nano-shaped crystals with increased surface area with increasing level of Zn-dopant. X-ray diffraction and Raman studies confirmed the films are composed of a single phase Mn_3O_4 tetragonal crystals with a typical spinel structure. The crystallite sizes and strain values were evaluated using Williamson Hall model and the result shows that grain size demonstrated an inverse and direct proportionality to microstrain and grain sizes of Mn_3O_4 film. Optical studies revealed the deposited films have fair transmittance to the visible light and the transmittance declined at higher level of Zn content, indicating good and enhanced photoabsorption. Mn_3O_4 film electrical conductivity were also found improving at higher level of Zn content. Enhanced electrochemical performance of the host electrode film was established with the incorporation of the Zn-dopant metal, indicating the Zn-ion involvement has improved the supercapacitive performance of electrofabricated Mn_3O_4 thin film electrode. The results therefore indicated successful electrosynthesis of Mn_3O_4 thin film. It also unveiled various surface properties suitable for photoabsorption, charge transport, separation and storage properties of Mn_3O_4 thin film can be improved with the incorporation of Zn particle. They also unveiled the materials properties suitable for enhanced optoelectronic and supercapacitive performance thereby capable of mitigating the world energy crises.

Declaration of competing interest

The authors declare no conflict of interest and that we have no financial of personal relationships with other people or organizations that can inappropriately affect this work. Thank you.

Data availability

Data will be made available on request.

Acknowledgment

The authors are thankful to the Department of Chemical Sciences, Fountain University, Osogbo, Osun State for their supports on the samples' syntheses. We also grateful to Prof. B.A. Taleatu of Department of Physics and Engineering Physics, Obafemi Awolowo University, Ile-Ife for his mentorship assistances and accessibility to his Optoelectronic and Energy Reaseach Laboratory for electrochemical measurements and analyses.

References

Adewinbi, S.A., Buremoh, W., Owoeye, V.A., Ajayeoba, Y.A., Salau, A.O., Busari, H.K., Tijani, M.A., Taleatu, B.A., 2021a. Preparation and characterization of TiO2 thin film electrode for optoelectronic and energy storage potentials: Effects of Co incorporation. Chem. Phys. Lett. 779, 138854. http://dx.doi.org/10.1016/j.cplett.2021.138854.

Adewinbi, S.A., Busari, R.A., Adewumi, O.E., Taleatu, B.A., 2021b. Effective photoabsorption of two-way spin-coated metal oxides interfacial layers: Surface microstructural and optical studies. Surf. Interfaces 23, 101029. http://dx.doi.org/10.1016/j.surfin.2021.101029.

Adewinbi, S.A., Busari, R.A., Animasahun, L.O., Omotoso, E., Taleatu, B.A., 2021c. Effective pseudocapacitive performance of binder free transparent α-V2o5 thin film electrode: Electrochemical and some surface probing. Physica B Condens. Matter. 621, 413260. http://dx.doi.org/10.1016/j.physb.2021.413260.

Adewinbi, S., Maphiri, V., Marnadu, R., Shkir, M., Alsdran, N.M.H., Algarni, H., Sujithkumar, G., Taleatu, B., Niyitanga, T., Kim, H., 2023. Transparent, photosensitive and highly efficient pseudocapacitive binder-free Mo-modified NiO thin film electrode for bifunctional optoelectronic and energy storage applications. J. Alloys Compd. 937, 168304. http://dx.doi.org/10.1016/j.jallcom.2022.168304.

Adewinbi, S.A., Maphiri, V.M., Taleatu, B.A., Marnadu, R., Manthrammel, M.A., Gedi, S., 2022a. Improved photoabsorption and refined electrochemical properties of pseudocapacitive CuxO thin film electrode with Zn incorporation for applications in optoelectronic and charge storage. J. Alloys Compd. 897, 163151. http://dx.doi.org/10.1016/j.jallcom.2021.163151.

Adewinbi, S.A., Maphiri, V.M., Taleatu, B.A., Marnadu, R., Manthrammel, M.A., Gedi, S., 2022b. Improved photoabsorption and refined electrochemical properties of pseudocapacitive CuxO thin film electrode with Zn incorporation for applications in optoelectronic and charge storage. J. Alloys Compd. 897, 163151. http://dx.doi.org/10.1016/j.jallcom.2021.163151.

Adewinbi, S.A., Maphiri, V.M., Taleatu, B.A., Marnadu, R., Shkir, M., Hakami, J., Kim, W.K., Gedi, S., 2022c. Binder-less fabrication, some surface studies, and enhanced electrochemical performance of Co, Cu-embedded MnO2 thin film electrodes for supercapacitor application. Ceram. Int. 48, 26312–26325. http://dx.doi.org/10.1016/j.ceramint.2022.05.315.

Adewinbi, S.A., Taleatu, B.A., Busari, R.A., Adewumi, O.E., Omotoso, E., Oyedotun, K.O., Manyala, N., 2020. Preparation and surface characterization of nanostructured MoO3/CoxOy and V2o5/CoxOy interfacial layers as transparent oxide structures for photoabsorption. J. Electron. Mater. 49, 3837–3848. http://dx.doi.org/10.1007/s11664-020-08096-9.

Adewinbi, S.A., Taleatu, B.A., Busari, R.A., Maphiri, V.M., Oyedotun, K.O., Manyala, N., 2021d. Synthesis and electrochemical characterization of pseudocapacitive α-MoO3 thin film as transparent electrode material in optoelectronic and energy storage devices. Mater. Chem. Phys. 264, 124468. http://dx.doi.org/10.1016/j.matchemphys.2021.124468.

Ahmed, R., Nabi, G., 2021. Enhanced electrochemical performance of Cr-doped NiO nanorods for supercapacitor application. J. Energy Storage 33, 102115. http://dx.doi.org/10.1016/j.est.2020.102115.

Ali, H.M., El-Aal, M.A., Al-Hossainy, A.F., Ibrahim, S.M., 2022. Kinetics and mechanism studies of oxidation of dibromothymolsulfonphthalein toxic dye by potassium permanganate in neutral media with the synthesis of 2-bromo-6-isopropyl-3-methyl-cyclohexa-2, 5-dienone. ACS Omega 7, 16109–16115. http://dx.doi.org/10.1021/acsomega.2c01462.

Bayram, O., Ertargin, M.E., Igman, E., Guney, H., Simsek, O., 2018. Synthesis and characterization of Zn-doped Mn_3O_4 thin films using successive ionic layer adsorption and reaction technique: Its structural, optical and wettability properties. J. Mater. Sci., Mater. Electron. 29, 9466–9473. http://dx.doi.org/10.1007/s10854-018-8980-9.

Busari, R.A., Taleatu, B.A., Adewinbi, S.A., Adewumi, O.E., Omotoso, E., Oyedotun, K.O., Fasasi, A.Y., 2020. Synthesis and surface characterization of electrodeposited quaternary chalcogenide Cu2ZnxSnyS1+ x+ 2y thin film as transparent contact electrode. Bull. Mater. Sci. 43, 1–9. http://dx.doi.org/10.1007/s12034-019-2030-y.

Chaudhary, M., Singh, M., Kumar, A., Gautam, Y.K., Malik, A.K., Kumar, Y., Singh, B.P., 2021. Experimental investigation of Co and Fe-doped CuO nanostructured electrode material for remarkable electrochemical performance. Ceram. Int. 47, 2094–2106. http://dx.doi.org/10.1016/j.ceramint.2020.09.042.

Chen, Z., Jiao, Z., Pan, D., Li, Z., Wu, M., Shek, C.H., Wu, C.L., Lai, J.K., 2012. Recent advances in manganese oxide nanocrystals: Fabrication, characterization, and microstructure. Chem. Rev. 112, 3833–3855. http://dx.doi.org/10.1021/cr2004508.

Dubal, D.P., Dhawale, D.S., Salunkhe, R.R., Lokhande, C.D., 2010. A novel chemical synthesis of Mn3O4 thin film and its stepwise conversion into birnessite MnO2 during super capacitive studies. J. Electroanal. Chem 647, 60–65. http://dx.doi.org/10.1016/j.jelechem.2010.05.010.

Ghosh, S.K., 2020. Diversity in the family of manganese oxides at the nanoscale: From fundamentals to applications. ACS Omega 5, 25493–25504. http://dx.doi.org/10.1021/acsomega.0c03455.

Greenwood, N.N., Earnshaw, A., 2012. Chemistry of the Elements. Elsevier.

Ibrahim, S.M., Al-Hossainy, A.F., Saha, B., Abd El-Aal, M., 2022. Removal of bromothymol blue dye by the oxidation method using KMnO4: Accelerating the oxidation reaction by Ru (III) catalyst. J. Mol. Struct. 1268, 133679. http://dx.doi.org/10.1016/j.molstruc.2022.133679.

Ibrahim, S.M., Al-Hossainy, A.F., Zoromba, M.S., El Azab, I.H., 2021. Base-catalyzed oxidation of sugarcane molasses by potassium ferricyanide in alkaline solutions. Int. J. Chem. Kinet. 53, 1101–1112. http://dx.doi.org/10.1002/kin.21517.

Jha, A., Thapa, R., Chattopadhyay, K.K., 2012. Structural transformation from Mn3O4 nanorods to nanoparticles and band gap tuning via Zn doping. Mater. Res. Bull. 47, 813–819. http://dx.doi.org/10.1016/j.materresbull.2011.11.057.

Kim, K.J., Park, Y.R., 2004. Sol–Gel growth and structural and optical investigation of manganese-oxide thin films: Structural transformation by Zn doping. J. Cryst. Growth 270, 162–167. http://dx.doi.org/10.1016/j.jcrysgro.2004.06.019.

Kocyigit, A., 2018. Structural, optical and electrical characterization of Mn3O4 thin films via Au composite. Mater. Res. Express 5, 066422. http://dx.doi.org/10.1088/2053-1591/aacb0d.

Larbi, T., Lakhdar, M.H., Amara, A., Ouni, B., Boukhachem, A., Mater, A., Amlouk, M., 2015. Nickel content effect on the microstructural, optical and electrical properties of p-type Mn3O4 sprayed thin films. J. Alloys Compd. 626, 93–101. http://dx.doi.org/10.1016/j.jallcom.2014.11.088.

Mohamed, N.S., Ahmed, M.M., Yahia, A., Ibrahim, S.M., Al-Hossainy, A.F., 2022. Development of azithromycin–Pd mono nanocomposite: Synthesis, physicochemical, characterization and TD-DFT calculations. J. Mol. Struct. 1263, 133126. http://dx.doi.org/10.1016/j.molstruc.2022.133126.

Nwanya, A.C., Awada, C., Obi, D., Raju, K., Ozoemena, K.I., Osuji, R.U., Ruediger, A., Maaza, M., Rosei, F., Ezema, F.I., 2017. Nanoporous copper-cobalt mixed oxide nanorod bundles as high performance pseudocapacitive electrodes. J. Electroanal. Chem. 787, 24–35. http://dx.doi.org/10.1016/j.jelechem.2017.01.031.

Owoeye, V.A., Ajenifuja, E., Adeoye, E.A., Salau, A.O., Adewinbi, S.A., Akindadelo, A.T., Pelemo, D.A., Popoola, A.P.I., 2022. Effect of precursor concentration on corrosion resistance and microstructure of ZnO thin films using spray pyrolysis method. Sci. Afr. 15, e01073. http://dx.doi.org/10.1016/j.sciaf.2021.e01073.

Owoeye, V.A., Ajenifuja, E., Adeoye, E.A., Salau, A.O., Akindadelo, A.T., Pelemo, D.A., Popoola, A.P.I., 2021. Microstructure and anti-corrosion properties of spray pyrolyzed Ni-doped ZnO thin films for multifunctional surface protection applications. Eng. Res. Express 3, 025012. http://dx.doi.org/10.1088/2631-8695/abf65f.

Owoeye, V.A., Ajenifuja, E., Babatope, B., G.A. Osinkolu, G.A., Popoola, A.P.I., Popoola, O., 2019. Experimental investigation and numerical simulation of mechanical properties and thermal stability of tin alloy processed by equal channel angular extrusion (ECAE). Eng. Res. Express 1, 025030. http://dx.doi.org/10.1088/2631-8695/ab52dd.

Panta, G.P., Subedi, D.P., 2012. Electrical characterization of aluminum (Al) thin films measured by using four-point probe method. KUSET 8, 31–36. http://dx.doi.org/10.3126/kuset.v8i2.7322.

Ponnar, M., Sathya, M., Pushpanathan, K., 2020. Enhanced UV emission and supercapacitor behavior of Zn doped CeO2 quantum dots. Chem. Phys. Lett. 761, 138087. http://dx.doi.org/10.1016/j.cplett.2020.138087.

Ran, R., Wu, X., Weng, D., Fan, J., 2013. Oxygen storage capacity and structural properties of Ni-doped LaMnO3 perovskites. J. Alloys Compd. 577, 288–294. http://dx.doi.org/10.1016/j.jallcom.2013.05.041.

Ristić, M., Musić, S., Popović, S., Dragčević, Đ., Marciuš, M., Ivanda, M., 2013. Synthesis and long-term phase stability of Mn3O4 nanoparticles. J. Mol. Struct. 1044, 255–261. http://dx.doi.org/10.1016/j.molstruc.2012.11.023.

Shano, A.M., Habeeb, A.A., Khodair, Z.T., Adnan, S.K., 2021. Effects of thickness on the structural and optical properties of Mn3O4 nanostructure thin films. In J. Phys. Conf. Ser. 1818, 012049. http://dx.doi.org/10.1088/1742-6596/1818/1/012049.

Sim, C.K., Majid, S.R., Mahmood, N.Z., 2021. ZnSnO3/mesoporous biocarbon composite towards sustainable electrode material for energy storage device. Microchem. J. 164, 105968. http://dx.doi.org/10.1016/j.microc.2021.105968.

Suib, S.L., 2008. Structure, porosity, and redox in porous manganese oxide octahedral layer and molecular Sieve materials. J. Mater. Chem. 18, 1623–1631. http://dx.doi.org/10.1039/B714966M.

Taleatu, B.A., Cozzarini, L., Olofinjana, B., Bertolini, G., Adewinbi, S.A., Behrendt, S., 2018. Preparation of nanocrystalline ZnO/CoxOy and CNT/CoxOy bilayers for photoabsorption potential: XPS and some surface structural characterization. Mater. Sci. Semicond. Process 87, 155–161. http://dx.doi.org/10.1016/j.mssp.2018.07.012.

Xu, J.F., Ji, W., Shen, Z.X., Li, W.S., Tang, S.H., Ye, X.R., Jia, D.Z., Xin, X.Q., 1999, Raman spectra of CuO nanocrystals. J. Raman Spectrosc. 30, 413–415. http://dx.doi.org/10.1002/(SICI)1097-4555(199905)30:5%3C413::AID-JRS387%3E3.0.CO;2-N.

Xu, H.Y., Le Xu, S., Li, X.D., Wang, H., Yan, H., 2006. Chemical bath deposition of hausmannite Mn3O4 thin films. Appl. Surf. Sci. 252, 4091–4096. http://dx.doi.org/10.1016/j.apsusc.2005.06.011.